Laser & Photonics Reviews

LASER & PHOTONICS REVIEWS

www.lpr-journal.org

RESEARCH ARTICLE OPEN ACCESS

In Situ Acoustic Monitoring of Focused Femtosecond Pulse Duration in Air

Indrė Meškėlaitė[1] | Hsin-Hui Huang[2] | Haoran Mu[2] | Nguyen Hoai An Le[2] | Tomas Katkus[2] | Edvinas Aleksandravičius[1] | Gabrielius Kontenis[1] | Domas Paipulas[1] | Saulius Juodkazis[1,2] | Darius Gailevičius[1]

[1]Laser Research Center, Faculty of Physics, Vilnius University, Vilnius, Lithuania | [2]Optical Sciences Centre, Swinburne University of Technology, Hawthorn, Victoria, Australia

Correspondence: Saulius Juodkazis (SJuodkazis@swin.edu.au) | Darius Gailevičius (Darius.Gailevicius@ff.vu.lt)

Received: 26 March 2026 | **Revised:** 7 April 2026 | **Accepted:** 8 April 2026

Keywords: acoustic pressure | chirp control | femtosecond | plasma temperature | pulse compression

ABSTRACT

The monitoring of the acoustic amplitude of an air breakdown at the focus of the femtosecond laser pulse was used to determine the pulse duration using a computer microphone. Pulse duration was tuned using the chirp settings of a femtosecond laser and measured by an autocorrelator before the focusing optics, where the ~241 fs pulses were compressed down to ~50 fs (n^2-Photonics compression unit). The amplitude of the acoustic signal scaled with the pulse duration t_p as $\propto 1/\sqrt{t_p}$ in the range from 50 fs to 2 ps. The acoustic signal showed $\propto E_p^{3/2}$ dependence on the pulse energy E_p, which was the same for the shortest (50 fs) and longer (250 fs) pulses widely used in laser machining and 3D nano/microprinting. This scaling is consistent with the electron–ion scattering defined by the electron temperature in the air breakdown plasma $T_e^{3/2}$. The demonstrated principle that the sound of air breakdown can be used to measure the pulse duration (50 fs–5 ps) is promising for femtosecond laser pulses at different wavelengths, where second-harmonic autocorrelators are not available.

1 | Introduction

Measurement of the duration of ultra-short pulses is based on the second harmonic generation (SHG), for example, by intensity autocorrelation or frequency-resolved optical gating (FROG), which retrieves phase and amplitude of the spectral components required for the determination of the temporal pulse length [1–4]. Measuring the pulse duration of shorter wavelength pulses presents obvious challenges due to the lack of efficient SHG media and detectors, especially when the doubled frequency pulses fall into the ultraviolet (UV) spectral range. Knowledge of the precise pulse duration is indispensable for ablation research and the determination of the ablation pressure P_{ab} [5], material removal rates [6–8], the relative contribution of ablation versus melting or amorphization rates [9–11], and the understanding of fs-laser-induced phase transitions [12–15], for example, formations of diaphite nano-diamonds and graphitization inside diamond [16, 17]. All key characteristics of light–matter interaction and energy deposition are related to the laser pulse intensity, and hence depend on the pulse duration t_p [18, 19]. Since the duration of femtosecond pulses directly governs peak intensity, ablation thresholds, and ultrafast phase transitions, it is a decisive parameter for controlling the formation of sub-microscopic structures during laser machining and nano/micro-printing [20].

Using sub-100 fs pulses is especially interesting for novel structuring contexts. For example, shifting to ultrashort pulse durations, such as 30 fs, fundamentally transitions the laser–matter interaction from a thermal (stochastic) regime to a

non-thermal (deterministic) regime, enabling ablation without the formation of Heat Affected Zones (HAZ). This precise energy deposition preserves the material's original phase, as seen in diamond processing, where, specifically 30 fs, pulses maintain the sp^3 crystal structure and achieve ultra-high precision surface roughness ($R_a < 0.1$ μm) impossible with longer pulses [21]. In nanostructuring of metals like zinc, shorter pulses favor Coulomb explosion over melting, allowing for the growth of distinct, fine-scale nanostructures that lose definition and merge at longer durations [22]. Also, in the same context, the higher peak intensities associated with shorter pulses generate immense localized shock pressures—calculated at nearly 800 GPa for 30 fs pulses compared to roughly 60 GPa for 550 fs pulses—which significantly enhances surface hardness [22]. Finally, in transparent materials like fused silica, reducing the pulse duration enlarges the favorable parametric window for writing complex internal features, such as nanoplanes, by stabilizing the threshold difference between desired modification and collateral damage [23]. This is well understood and appreciated in the laser fabrication community that, with shortening pulses, the physical and technological modes of interaction become more favorable for achieving micro- to nano-scale features, and followed by new induced properties.

The use of such radiation is often facilitated by focusing. Any energy deposition in the focal volume by definition generates pressure, that is, 1 J/m^3 = 1 N/m^2 ≡ 1 Pa. This fundamental principle underlies photoacoustics, which has become a widely used technology across various fields, including communications and biomedical tomography [24–27]. Laser ablation and machining of the surface or within the bulk of a material can be characterized by the resulting pressure and, consequently, sound generation [28–30], which is used to control and monitor laser machining [31]. Early studies of high-intensity ablation [32–34] have shown that hot electrons have the major contribution to ablation pressure $P_{ab} = 93 t_p^{-1/3}(1 - f_i)\eta^{0.67} I_L^{0.93} \lambda_L^{0.52}$ as compared to thermal electron-driven ablation $P_{ab} \propto (\eta I_L)^{2/3}$, where I_L (PW/cm^2) is the laser pulse intensity, η is the absorption ratio, λ_L (μm) is the laser wavelength, $f_i \approx 0.5$ is the energy loss factor due to fast ions, and t_p (ns) is the pulse duration. The experimental determination of the ablation pressure was based on momentum conservation between the ablation plasma and the target mass m (neglecting the ablated ion mass) on a pendulum of length l: $P_{ab} = \frac{m}{t_p S}\sqrt{\frac{g}{l}} X_a$, where X_a is the arc length of the quarter period, g is the gravitational constant, and S is the area of energy deposition [32]. It was demonstrated that the mechanical coupling coefficient $C_m \equiv P_{ab}/I_L$, determined experimentally, follows within a factor of two the same scaling versus $I_L \lambda \sqrt{t_p}$ over a range of seven orders of magnitude for pulse duration from ms-to-ns [35]. This trend is based on the electron density n_e scaling as $\propto I_L/(I_L \lambda \sqrt{t_p})^{3/4}$ [35]. The ablation pressure is important in the laser peening of metals to improve their mechanical and anticorrosive properties [36], and requires precise knowledge of the energy deposition per area and pulse duration, as well as the deposition volume for transparent materials and phase transitions.

For ultra-short sub-1 ps laser pulses at high intensities, tunneling and multi-photon ionization become prevalent mechanisms in fast electron removal from the irradiated surface. Under such conditions, the ablation threshold, which is the removal of ions, can be reduced as less energy is required to disintegrate the material surface. Indeed, the ablation threshold is proportional to the sum of the ionization potential J_i (dielectrics) or the electron work function w_e (metals) and the binding energy ϵ_b (enthalpy of vaporization) [37]. Once high-energy electrons are removed from the surface of the material (exceeding J_i or w_e), the charged surface disintegrates at a smaller energy per atom than ϵ_b; that is, ablation is facilitated by the Coulomb explosion [38]. The reduction of the ablation threshold was experimentally determined for dielectrics for sub-10 fs pulses [39] where Coulomb explosion is more probable. For metals, the reduction of the ablation threshold was not unambiguously confirmed. Wavelength independence in ablation of dielectrics is another trait for ultra-short laser pulses [40].

A broad field of photoacoustics, where localized heating or even ablation is applied, can benefit from control of pulse duration. One notable application is light-induced breakdown spectroscopy (LIBS) [41], in which plasma formation by high-intensity pulsed lasers has been developed into a spectroscopic technique. Such methods can benefit from acoustic monitoring of energy deposition [42] and have even been tested under Martian exploration conditions [43]. The field of photoacoustics, which originated in 1880, has since evolved into a major biomedical imaging technique [44]. Beyond applied photoacoustics, acoustic analysis is also useful as a probe of ultrafast energy deposition and plasma dynamics. Real-time in situ acoustic monitoring has been used to study microplasma formation and filamentation in tightly focused femtosecond irradiation of silica glass [45], while in tightly focused air breakdown, shockwave-induced density gradients were shown to affect secondary THz and X-ray emission [46]. Acoustic characterization of laser filamentation in air has revealed a two-photon Raman excitation mechanism [47], while shock-wave generation in air [48] and from ablated metal surfaces [49] has been investigated using laser beam deflection. Acoustic emissions from air breakdown are higher for nanosecond than for picosecond pulses, indicating a greater conversion efficiency of optical to mechanical (acoustic) energy [50], a trend also observed in water [51]. Cylindrical shock waves generated by femtosecond laser pulses can be visualized in supersaturated vapor through induced precipitation, as recently demonstrated in 3D optical cloud displays [52]. Acoustic signatures of such shock waves can reveal details of laser–matter interactions during the early energy deposition and shock–cavitation stages. Indeed, acoustic monitoring protocols are already established in laser machining [53].

Here, an acoustic method for determining pulse duration is introduced, based on the acoustic detection of air breakdown using a computer USB microphone. We implemented a multi-pass pulse compressor (n^2-Photonics) which is capable of compressing pulses down to 50 fs with one unit and down to 10 fs with two units, provided the broad spectrum of the initial pulse; we used only one stage of compression, down to ∼50 fs in this study.

2 | Experimental

The schematics of the experiment are shown in Figure 1. Fs-laser pulses of the shortest t_p = 241 fs duration (at the objective

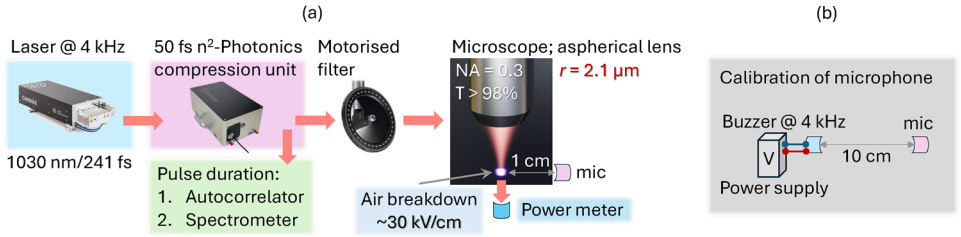

FIGURE 1 | Acoustic monitoring of air breakdown. (a) A pulse compression unit (n^2-Photonics) was used to shorten pulse duration from 241 to 50 fs. The acoustic amplitude of air breakdown was recorded at the 4 kHz laser repetition rate and analyzed via the repetition-frequency component and its harmonics. (b) The microphone was calibrated using a buzzer/transducer.

lens) were chirp-controlled by laser settings to provide pulse durations in a wide range of 0.25–2 ps. The fs-laser output was guided through the multipass cell pulse compression unit (model MIKS1_S, n^2-Photonics GmbH). The output was monitored using a spectrometer and steered into the laser machining setup by reflective optical elements. Laser pulses focused with an aspheric lens ($NA = 0.3$) produced a spark in the air under the breakdown conditions ~30 kV/cm. Because filamentary laser-plasma sources in air are spatially extended and their detected acoustic waveform evolves with propagation distance, the present experiments used tight focusing and a fixed 1 cm microphone distance so that the source could be treated approximately as localized to the focal volume [57]. If the entire maximum incident pulse energy of 50 µJ (up to the maximum used) is conservatively assumed to be absorbed in air, then the maximum radius of the shock-compressed region can be estimated as [58]

$$r_{\mathrm{sh,max}} = \left(\frac{3E_p}{4\pi p_0}\right)^{1/3},$$

where E_p is the deposited (absorbed) pulse energy and p_0 is the ambient static air pressure. For $E_p = 50$ µJ and $p_0 = 1$ bar, this gives

$$r_{\mathrm{sh,max}} \approx 490\ \mu\mathrm{m}.$$

Since the microphone was placed 1 cm from the focal volume, the detector distance exceeds this conservative upper-bound shock-transition scale by more than an order of magnitude. Therefore, the recorded signal is interpreted as the propagated acoustic response rather than the near-field shock profile, and resolving the temporal structure of the initial shockwave is not required for the relative amplitude-based monitoring used here.

A detachable computer microphone (GXT 210 Gaming USB Microphone, Trust International B.V.) was used for the acoustic monitoring of the signal amplitude (a computer readout of the amplitude was used, and the response dependence was tested with a calibrated buzzer; see Section A1.3). An autocorrelator (Geco, Light Conversion) was set before the focusing optics, as shown in Figure 1a, to measure the pulse duration directly at the relevant pulse energy while avoiding detector damage; it was verified that pulse propagation through the aspheric lens leads to insignificant elongation of the compressed pulse via the spectrum. The pulse energy was measured before and after the objective lens to account for its transmittance. During measurements after the objective lens, however, measurements were carried out without and with plasma present. The power meter was temporarily inserted beyond the focal plane to determine the incident pulse energy delivered to the focal volume, and was removed from the beam path during acoustic measurements. In this way, the reported pulse energies correspond to the energy incident at focus under the experimental conditions used for sound detection. Even under breakdown conditions, the generated plasma in air remains strongly under-dense with respect to the critical plasma density at 1030 nm ($n_{e,\mathrm{crit}} \approx 1 \times 10^{21}$ cm^{-3}). For the maximum pulse energies used in this study (≤ 50 µJ, focused by $NA = 0.3$ lens), the plasma density is in the range of 10^{17}–10^{18} cm^{-3}, which corresponds to less than 0.1 % absorption at the fundamental wavelength. Hence, plasma absorption is negligible compared with the shot-to-shot fluctuations, and does not influence the reported scaling of the acoustic signal.

Figure 2a shows a photograph of the actual setup. Acoustic monitoring was carried out using the mobile phone app phyphox [54–56]; the inset shows the peak acoustic signal at ~4 kHz, which is the peak sensitivity of the microphone and was used for setting the laser repetition rate. For calibration of the microphone, a piezoelectric buzzer (PK-12N40PE-TQ, Hitpoint Inc.) was placed 10 cm away from the microphone and driven at a fixed voltage of 10 V using a power supply unit (Figure 1b). Under these conditions, the amplitude of a sound wave is related to the sound pressure of $L_p = 80$ dB; here $L_p = 20\log_{10}[p/p_0]$, with p (Pa) being the root mean square (RMS) sound pressure and $p_0 = 20$ µPa is the threshold of human hearing. Hence, an amplitude of 100 dB corresponds to a sound pressure of 2 kPa.

3 | Results

The ionization of air depends on the electrical field strength, that is, the intensity of the laser pulse. For the same pulse energy E_p, a shorter laser pulse duration t_p results in a higher peak intensity $I_p = 2E_p/(t_p S_p)$, where E_p is the pulse energy, S_p is the focal spot area. The factor of 2 links the average energy (or fluence) with the peak amplitude, considering a Gaussian-like intensity envelope, which is an approximation that is more critical for the ultra-short laser pulses. The air breakdown at the field strength of ~30 kV/cm in air (room conditions) can be used to measure the pulse intensity using an acoustic transducer, as was shown for lens-focused (focal length $f = 100$ mm) 800 nm/50 fs pulse filaments in air [46]. In this study, tighter focusing was used to avoid filamentation, which introduces ambiguity in the spatial position of the sound source when the acoustic sensor (microphone) has a detection surface with a cross section comparable to (or smaller than) the length of the filament [59, 60].

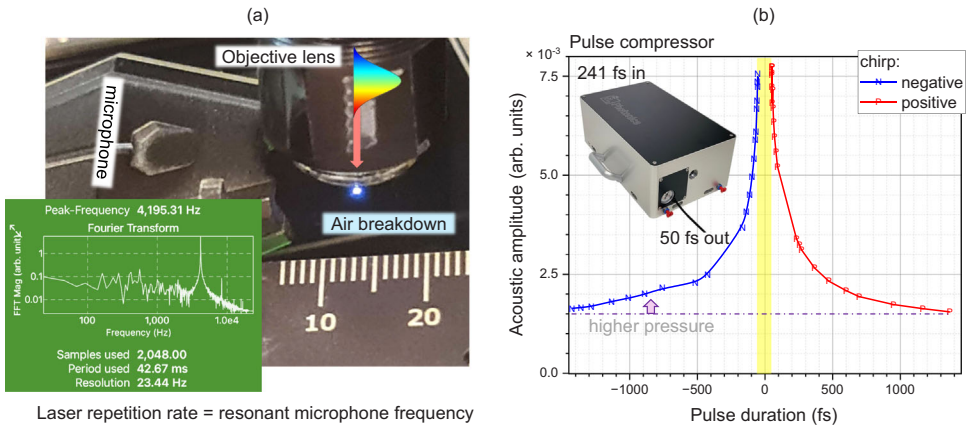

FIGURE 2 | (a) Experimental setup: the objective lens ($NA = 0.3$) with a microphone placed at a 1 cm distance from the focus. The inset on the left shows the Fourier transform spectrum of the air breakdown at 4 kHz laser repetition rate acquired using the Audio Spectrum function in the phyphox phone app, available for Android and iOS, www.phyphox.org [54–56]. (b) The acoustic amplitude (microphone's output) as a function of pulse duration. The pulse duration of the fs-laser (Carbide) was measured using a scanning autocorrelator (Geco, Light Conversion), after the pulse had passed through the compression unit (n^2-Photonics; as shown in the inset).

3.1 | Spark-Acoustics for Measurements of Pulse Duration

The fs-laser pulse duration was set using the positive and negative chirp with the laser (Carbide) compressor via software controls. Then, the ultrashort pulse from the fs laser passes through the pulse compression unit (n^2-Photonics) and is focused in air with an objective lens. The acoustic signature of air breakdown at the focus is measured using a microphone placed 1 cm from the spark. The pulsed beam autocorrelation functions were measured before the focusing optics, and the beam spectrum was measured before and after the focusing optics to confirm there was no detectable change in the spectrum. All measurements were collected to be referenceable with the acoustic signal.

Figure 2b shows the result of the acoustic signal in arbitrary units (see details of calibration below in Section 3.2) versus the pulse duration for the positive and negative chirp settings. The laser operated at a 4 kHz repetition rate, and the recorded acoustic signal exhibited a clear component at the repetition frequency together with its harmonics, which were used for analysis (see inset on the left in Figure 2a). The shortest pulse duration of $t_p \approx 52.5$ fs was achieved before the objective lens using the pulse compression unit. For the longer pulses (chirped by Carbide's compressor), the acoustic amplitude (sound pressure) was slightly higher for the negatively chirped pulses compared to those obtained by a positive chirp (arrow in Figure 2b). This is consistent with a stronger contribution of multiphoton ionization at the shorter wavelengths at the incoming front of the laser pulse (the negative chirp). Then, avalanche ionization is favored at longer wavelengths (trailing end of the pulse) as $\propto \lambda^2$ when the free charge carriers are already created by multiphoton ionization at the blue-wavelength front of the pulse [37].

Spectral monitoring of the output of the pulse compression unit (n^2-Photonics) was carried out to measure the spectrum of the compressed pulses, which were chirp-controlled by the laser setting (Figure 3a). For illustration, a couple of spectra for the positive and negative chirp settings (Carbide) are shown along with the spectral bandwidth-limited output of the fs-laser (Carbide) before compression at the n^2-Photonics pulse compression unit with the nominal 241 fs pulse duration. The broadest spectra corresponded to the ~50 fs pulse measured before the objective lens.

Figure 3b shows the acoustic signal measured with the microphone for the positive chirp branch (Figure 2b) on a log–log scale. The slope of acoustic amplitude, which is the sound pressure, was decreasing with pulse duration as $\sim 1/\sqrt{t_p}$. Thus, Figure 3b serves as the setup-specific calibration characteristic of the method: once the acoustic amplitude is referenced to independently measured pulse durations in a fixed geometry, subsequent changes in the acoustic signal can be interpreted as corresponding changes in pulse duration within that calibrated regime. These measurements were carried out 1 cm from the spark at a 4 kHz laser repetition rate. This scaling hints at the diffusion-related mechanism in the generation of an acoustical signal, that is, the sound pressure wave. The initial shock wave converts to a sound (pressure) wave at the distance r_s when the internal energy in the volume inside the shock front is comparable to the absorbed pulse energy E_{abs} [61], where, for air, the bulk modulus $B = 101$ kPa (isothermal; 142 kPa for isentropic) is used, $\frac{4}{3}\pi r_s^3 B = E_{abs}$. Even for the overestimated 20% absorbance at the maximum $E_{max} = 40$ μJ, the shock propagates only $r_s \approx \sqrt[3]{0.2E_{max}/(4B)} \approx 0.27$ mm, which is much smaller than the spark-to-microphone distance of 1 cm. When the distance to the microphone is much smaller, and pulse energies are higher, a more complex shock wave propagation has to be considered [62]; however, it was not required for this study.

3.2 | Calibration: Pulse Intensity to Sound Pressure

The audio signature of the fs-pulse-induced breakdown in air is analyzed using the Fast Fourier Transform (FFT) of the microphone output (amplitude). Figure 4a shows the audio spectrum taken by a mobile phone with a clear presence of up to

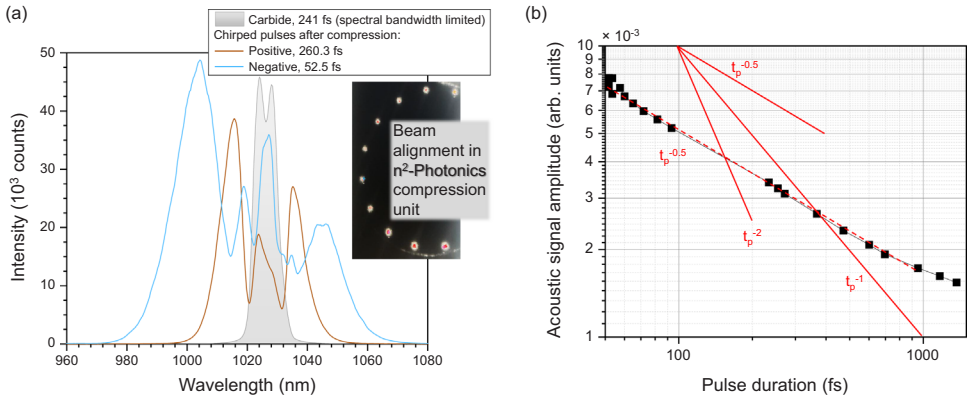

FIGURE 3 | (a) Spectra of compressed fs-laser (Carbide) pulses at the output of n^2-Photonics single stage pulse compression unit MIKS1_S at different chirp-settings of fs-laser (AvaSpec 3648 fiber optic spectrometer). As a reference, the spectrum of 241 fs reference measured at the laser output port is shown. The inset shows a screenshot of the n^2-Photonics compression unit alignment, where multiple reflection sites at fixed spatial positions inside a multipass cell for spectral pulse broadening are made with external beam steering. (b) The amplitude of the acoustic signal as a function of pulse duration measured at the focal region follows $\propto 1/\sqrt{t_p}$ dependence.

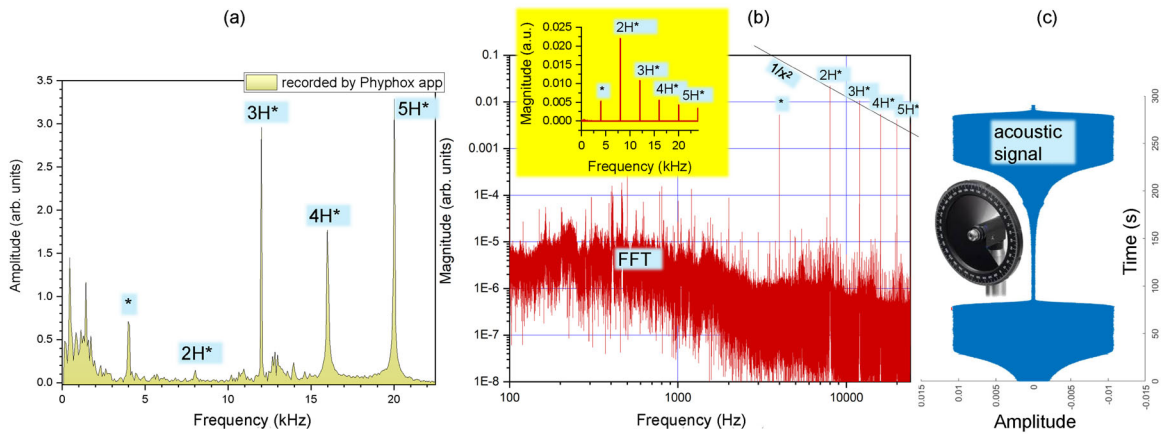

FIGURE 4 | Analysis of audio signal from laser-induced spark. (a) Audio for the shortest pulse recorded on a mobile phone app (phyphox) at ~10 cm from the spark, where the pulse duration was the shortest ~50 fs. The star-markers (*) show the fundamental and higher harmonics. (b) Amplitude of the FFT spectrum (presented in log–log scale) of the microphone signal placed 1 cm from the spark. The inset shows a linear scale of the FFT spectrum. (c) Automated recording of the acoustic signal (a raw time-dependent amplitude of all harmonics) when a neutral density filter was rotated by a motorized stage; the transient was measured for the shortest pulse.

four harmonics of the laser driving frequency at 4 kHz. The FFT of the microphone output when the microphone is at 1 cm distance away from the spark is shown in Figure 4b. Then, the amplitude of the fundamental frequency of 4 kHz and its harmonics (with the bandwidth window of ±0.1 kHz) was selected for the calibration. The microphone sensitivity is favorable in this frequency range (inset in Figure 2a). The amplitude of higher harmonics (2nd-to-5th) was decaying as $1/f^2$, where f is the frequency of sound. For the intensity calibration of sound amplitude, a neutral density filter was used at the selected pulse duration (Figure 4c). The acoustic amplitude was recorded at different intensities as the filter was rotated for different pulse durations set with laser pulse pre-chirping (Figure 5a). The averaged acoustic signal as a function of pulse energy is shown in Figure 5b. Clear scaling of the acoustic amplitude with pulse energy is obtained for the different pulse durations: the shortest and positively (P) or negatively (N) chirped ones. The power scaling of the acoustic amplitude is discussed next.

4 | Discussion

Figure 6 shows the evolution of the acoustic signal versus pulse energy at the 4 kHz laser repetition rate in a log–log scale in order to reveal the power scaling laws. At pulse energy of $E_p \approx 2$ μJ (depends on pulse duration t_p), a detectable acoustic signal emerges from the noise floor ~10^{-4} (specific to the USB microphone used). For the shortest pulse $t_p = 52.5$ fs, $E_p = 5$ μJ was the threshold from which the power scaling followed the slope of $\gamma_1 = 3/2$. This scaling applies to the intensity since the difference between acoustic signals at the same pulse energy but for ~50 and ~250 fs pulse durations was different by five times as expected. Similar scaling was observed for a loosely focused filament 800 nm/50 fs [46]; however, there was no self-focusing and filamentation at the used experimental conditions as discussed below. The most probable explanation of the observed scaling is due to momentum transfer time $\tau_{ee} \approx \tau_{ei}$ between electrons and ions, which for the Maxwellian velocity distribution

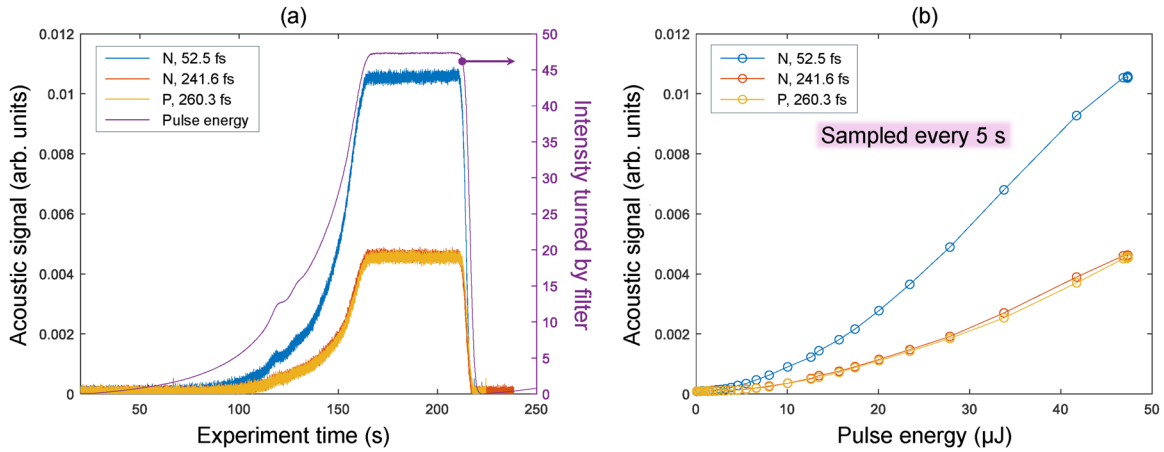

FIGURE 5 | Intensity scans. (a) Acoustic signal vs time of neutral density filter rotation at different negative (N) and positive (P) chirp settings. Also, pulse energy was measured. The color markers show the directly measured pulse duration before the objective lens. (b) Acoustic signal versus pulse energy for different pulse durations (chirp values set for fs-laser (Carbide)).

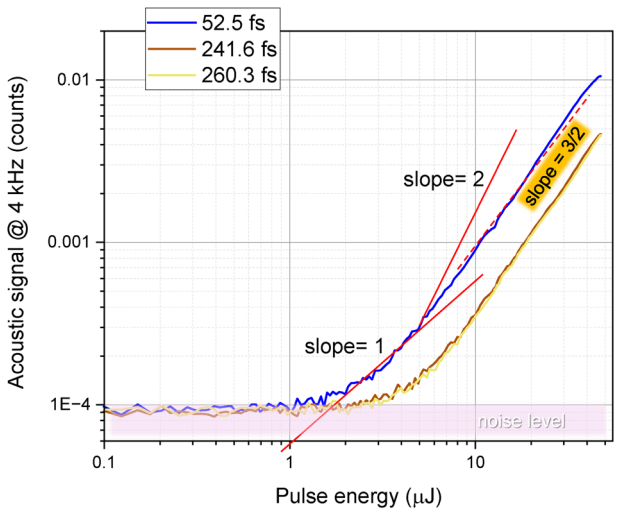

FIGURE 6 | Acoustic signal measured by a microphone placed at 1 cm from the air breakdown region of $NA = 0.3$, focused pulse of different duration and chirp (same as in Figure 5b only in log–log scale). For $E_p = 1$ μJ, $t_p = 50$ fs and beam waist (radius) $r = 2.1$ μm, the average intensity $I_p = 144.4$ TW/cm^2.

scales as $\tau_{ei} \propto (kT_e)^{3/2}$, where T_e is the electron temperature [63]. The frictional force on distribution of electrons drifting through stationary ions in z-direction at velocity v_z is $F_z = -n_e m_e \langle \nu_{ei} \rangle v_z$, where n_e is electron density and m_e is the electron mass. The average of the electron-ion collisional frequency is given by [63]

$$\langle \nu_{ei} \rangle = \frac{\sqrt{2} n_i Z^2 e^4 \ln \Lambda}{12\pi^{3/2} \varepsilon_0^2 \sqrt{m_e} T_e^{3/2}}, \tag{1}$$

where n_i is the ion density, Z the ionization charge state, e is the electron charge, $\ln \Lambda$ is the Coulomb logarithm of the plasma parameter Λ (the ratio of the maximum impact parameter to the classical distance of the closest approach in Coulomb scattering), and ε_0 is the vacuum permittivity. The momentum transfer time $\tau_{ei} \equiv 1/\langle \nu_{ei} \rangle \propto T_e^{3/2}$ and defines the power dependence of the acoustic (pressure) signal shown in Figure 6. The higher the laser pulse energy, the higher the temperature (and velocity v_e of electrons in plasma). The collision frequency varies with velocity as v^{-3}, the faster electrons collide less with ions.

Let us estimate conditions used for the highest pulse energy $E_p = 50$ μJ when the maximum of the acoustic signal reached a magnitude of 10^{-2} (100 times above the noise level; see Figure 6). The beam waist radius was $r = 2.1$ μm for the $NA = 0.3$ lens. The depth of focus is defined by double of the Rayleigh length $2z_R = 2\pi r^2/\lambda \approx 26.9$ μm. Hence, the axial extent of $t_p \approx 50$ fs pulse ($ct_p \approx 15$ μm) is all within the focal region since $ct_p \approx z_R$. The average fluence is $F_p = E_p/(\pi r^2) = 359.7$ J/cm^2 and intensity (irradiance) $I_p = F_p/t_p = 6.8$ PW/cm^2 for pulse duration $t_p = 52.5$ fs (the peak fluence is approximately by a factor of two larger). In air, the intensity clamping occurs at ~100 TW/cm^2 (depending on focusing NA) [64, 65], that is, at ~50× lower pulse energy.

Finally, the observed dependence can be expressed as

$$A_{ac}(t_p, E_p) \propto \frac{E_p^{3/2}}{\sqrt{t_p}},$$

where A_{ac} is the acoustic amplitude, t_p is the laser pulse duration, and E_p is the pulse energy. The $1/\sqrt{t_p}$ scaling originates from the increase in peak intensity, $I_p = 2E_p/(t_p \pi r^2)$, at shorter durations for a given focal spot. The $E_p^{3/2}$ scaling arises from electron–ion scattering dynamics in the air plasma (see Figure 6). Together, these relations define the core equation for acoustic determination of femtosecond pulse duration.

The slope of $\gamma_1 \approx 1.3$ in the power dependence of the acoustic signal in air from 800 nm/50 fs pulses focused to 0.2 mm focus (longitudinal extent) was recognizable at the onset of filamentation at 70–80 μJ/pulse, that is., the power per pulse ~1.5 ± 0.1 GW [46]. This average pulse power is lower by less than twice as compared with the critical power of self-focusing in dry air $P_{cr} \approx 2.4$ GW for 800 nm/50 fs pulses; the nonlinear refractive index of air is $n_2 \approx 4 \times 10^{-23}$ m^2/W. In the current study, the $\gamma_1 = 1.5$ was observed from ~5 μJ/pulse or 0.1 GW/pulse

(average). Hence, the self-focusing and intensity clamping should be excluded as important contributors to the air breakdown at the focus. Origin of the acoustic signal is the focal volume, where air breakdown plasma was formed and energy was deposited (see Section A1.3).

In the used average intensity range (0.14–7) PW/cm^2 (1–50 μJ/pulse), the electron temperature T_e upon irradiation of liquid and solid targets becomes very high and emission of soft and hard x-rays via bremsstrahlung is taking place and can be controlled by pulse duration and chirp [28, 66]. The power of emission is P_{br} (W/m^3)$\propto Z'^2 n_e n_i \sqrt{T_e}$, where $n_{e,i}$ is the electron and ion densities, respectively, and Z' is the ionization number.

Compared to conventional autocorrelation, which remains the standard for fs-pulse duration characterization [67], the acoustic method presented here offers distinct advantages and limitations. The main advantages are its simplicity (no need for nonlinear crystals or alignment), including spectral ranges where second harmonic generation is impractical, and suitability as an in situ monitoring tool during laser machining, where real-time drift of pulse duration may occur. It should be noted that while the absolute acoustic amplitude can be influenced by environmental conditions such as room acoustics and microphone positioning, the observed scaling laws, $A \propto 1/\sqrt{t_p}$ and $A \propto E_p^{3/2}$, are intrinsic to the plasma physics of air breakdown and remain robust. It should be noted that the absolute acoustic amplitude can be influenced by environmental conditions and detector geometry. In the present work, the observed scaling is supported for the investigated fixed-geometry regime, while the absolute calibration coefficient may depend on ambient and detection conditions. Therefore, the method is best applied in in situ scenarios, where the microphone and geometry are kept fixed during an experiment.

The main disadvantages are reduced precision compared to autocorrelation and the lack of full temporal profile retrieval (only relative scaling of duration is accessible). Thus, the acoustic method complements but does not replace autocorrelation; it enables pulse monitoring in regimes where traditional methods are impractical or unavailable.

5 | Application

The scaling law can be used to predict the pulse duration. For this, a calibration characteristic must be created as shown in Figure 3b. For each setup, the absolute amplitude offset might differ. The workflow is as follows. The acoustic amplitude is first measured in a fixed optical and acoustic geometry for a set of pulse durations t_p independently determined by the autocorrelator or any other absolute pulse-duration measurement tool. The corresponding acoustic amplitudes A_{ac} are then plotted against t_p in a log–log representation and fitted by a linear relation

$$\log A_{ac} = \alpha + \beta \log t_p, \tag{2}$$

which defines the method's setup-specific prediction characteristic. In the present case, the fitted slope is close to $\beta \approx -1/2$, consistent with the observed scaling $A_{ac} \propto 1/\sqrt{t_p}$.

For predictive use, the method should be applied only within the calibrated operating range: (i) the recorded acoustic signal must remain sufficiently above the ambient noise floor, after baseline subtraction, while preserving adequate dynamic range, and (ii) the pulse energy must lie in the regime where the acoustic response follows the linear slope in the log–log plot, as verified by the pulse-energy scaling in Figure 6. Under these conditions, a measured acoustic amplitude can be converted into the corresponding pulse duration through the inverse calibration relation

$$t_p = 10^{(\log A_{ac} - \alpha)/\beta}. \tag{3}$$

The reliability of the method is therefore limited by how accurately the acoustic-signal variation ΔA_{ac} can be determined in absolute and statistical terms. The number of samples of the raw acoustic trace $A_{ac}(t)$ required to obtain a reliable mean value depends on the detector, the recording circuit, and the ambient background. In the present work, the recordings were performed over a relatively macroscopic timescale, so the main practical uncertainty is associated with determining the baseline and plateau levels of the measured acoustic signal.

Thus, the method's reliability is primarily determined by the quality of the calibration line in Figure 3b, along with the practical uncertainty in determining the raw acoustic baseline and plateau level during signal acquisition. For a different experimental geometry or detector configuration, the same workflow should be repeated to obtain a new calibration characteristic.

6 | Conclusions and Outlook

In the present setup, acoustic monitoring was experimentally validated for pulse-duration tracking from 50 fs to 2 ps, with the highest sensitivity in the 50–500 fs range. The method is summarized by the working equation $A_{ac} \propto E_p^{3/2}/\sqrt{t_p}$, which provides a direct acoustic signature of pulse duration in the 50 fs–5 ps range at the focus (important for the sub-100 fs pulses, which can be strongly affected by dispersion of the beam delivery optics).

In this study, a common USB computer microphone was used 1 cm away from a micro-sized focal volume where air breakdown was induced by a focused ultra-short laser pulse. A pulse compression unit (n^2-Photonics) was implemented to achieve maximum compression of 1030 nm/241 fs pulses while their duration in the focus (after compressor) was chirp-tuned using the fs-laser source. Such a setup can be useful for laser machining applications and monitoring the sound for estimation of the pulse intensity or pulse duration, as well as their temporal drift during long experiments. Because laser-induced sub-microscopic structures depend sensitively on peak intensity—and therefore on pulse duration—the ability to monitor pulse length acoustically at the workpiece provides a practical tool for reliable studies of nano- and micro-structuring phenomena.

In its present form, the approach should be regarded as a practical relative in situ monitor, calibrated against autocorrelation. Further extension of this application for a two-stage compressor (n^2 Photonics) unit, which compresses pulses down to 10 fs, is a required research effort. Acoustic monitoring of pulse duration,

that is, intensity, can be practical for laser machining where the workpiece-laser beam interaction area/volume (intensity) is changing and can be acoustically monitored for the processing feedback. Extending acoustic monitoring to high 0.2–2 MHz frequencies as well as to the burst and biburst modes is required for practical applications of fs-laser machining.

Most notably, we expect this technique to be useful for characterization of sub-fs pulses as a black-box technique, without any concerns about the dispersion of relay optics, spectral bandwidth, or autocorrelation resolution, and any accommodating optics of the characterization technique. This is a true optics-free characterization approach.

Acknowledgements

S.J. acknowledges funding by the Australian Research Council Linkage LP220100153 and Discovery DP240103231 grants. D.G, E.A., and G.K. acknowledge funding from the Research Council of Lithuania (LMTLT), grant No. S-MIP-23-49. I.M. and D.P. acknowledge the "Universities–Excellence Initiative" programme by the Ministry of Education, Science and Sports of the Republic of Lithuania under the agreement with the Research Council of Lithuania (project No. S-A-UEI-23–6). The authors acknowledge technical discussions regarding the operation of the multi-pass cell compressor with Oleg Pronin.

Open access publishing facilitated by Swinburne University of Technology, as part of the Wiley - Swinburne University of Technology agreement via the Council of Australasian University Librarians.

Conflicts of Interest

The authors declare no conflict of interest.

Data Availability Statement

The data that support the findings of this study are available from the corresponding author upon reasonable request.

References

1. R. Trebino, K. W. DeLong, D. N. Fittinghoff, et al., "Measuring Ultrashort Laser Pulses in the Time-Frequency Domain Using Frequency-Resolved Optical Gating," *Review of Scientific Instruments* 68, no. 9 (1997): 3277–3295.

2. K. DeLong, R. Trebino, J. Hunter, and W. White, "Frequency-Resolved Optical Gating With the Use of Second-Harmonic Generation," *Journal of the Optical Society of America B* 11, no. 11 (1994): 2206–2215.

3. R. Jafari, T. Jones, and R. Trebino, "100% Reliable Algorithm for Second-Harmonic-Generation Frequency-Resolved Optical Gating," *Optics Express* 27, no. 3 (2019): 2112–2124.

4. A. Kwok, L. Jusinski, M. Krumbiigel, J. N. Sweetser, D. N. Fittinghoff, and R. Trebino, "Frequency-Resolved Optical Gating Using Cascaded Second-Order Nonlinearities," *IEEE Journal of Selected Topics in Quantum Electronics* 4, no. 2 (2002): 271–277.

5. L. Zhou, X. Y. Li, W. J. Zhu, J. X. Wang, and C. J. Tang, "The Effects of Pulse Duration on Ablation Pressure Driven by Laser Radiation," *Journal of Applied Physics* 117, no. 12 (2015): 125904.

6. B. Neuenschwander, B. Jaeggi, and M. Schmid, "From fs to Sub-ns: Dependence of the Material Removal Rate on the Pulse Duration for Metals," *Physics Procedia* 41 (2013): 794–801.

7. B. Lauer, B. Jäggi, and B. Neuenschwander, "Influence of the Pulse Duration Onto the Material Removal Rate and Machining Quality for Different Types of Steel," *Physics Procedia* 56 (2014): 963–972.

8. B. Jaeggi, B. Neuenschwander, S. Remund, and T. Kramer, "Influence of the Pulse Duration and the Experimental Approach Onto the Specific Removal Rate for Ultra-Short Pulses," in *Laser Applications in Microelectronic and Optoelectronic Manufacturing (LAMOM) XXII*, 10091 (SPIE, 2017), 105–114.

9. J. Bonse, S. Wiggins, and J. Solis, "Dynamics of Femtosecond Laser-Induced Melting and Amorphization of Indium Phosphide," *Journal of Applied Physics* 96, no. 4 (2004): 2352–2358.

10. P. Lorazo, L. J. Lewis, and M. Meunier, "Thermodynamic Pathways to Melting, Ablation, and Solidification in Absorbing Solids Under Pulsed Laser Irradiation," *Physical Review B–Condensed Matter and Materials Physics* 73, no. 13 (2006): 134108.

11. M. Garcia-Lechuga, N. Casquero, J. Siegel, et al., "Amorphization and Ablation of Crystalline Silicon Using Ultrafast Lasers: Dependencies on the Pulse Duration and Irradiation Wavelength," *Laser & Photonics Reviews* 18, no. 11 (2024): 2301327.

12. Y. Siegal, E. Glezer, L. Huang, and E. Mazur, "Laser-Induced Phase Transitions in Semiconductors," *Annual Review of Materials Science* 25, no. 1 (1995): 223–247.

13. I. Shumay and U. Höfer, "Phase Transformations of an InSb Surface Induced by Strong Femtosecond Laser Pulses," *Physical Review B* 53, no. 23 (1996): 15878.

14. A. Vailionis, E. Gamaly, V. Mizeikis, W. Yang, A. Rode, and S. Juodkazis, "Evidence of Superdense Aluminium Synthesized by Ultrafast Microexplosion," *Nature Communications* 2 (2011): 445.

15. M. Kandyla, T. Shih, and E. Mazur, "Femtosecond Dynamics of the Laser-Induced Solid-to-Liquid Phase Transition in Aluminum," *Physical Review B–Condensed Matter and Materials Physics* 75, no. 21 (2007): 214107.

16. P. S. Salter, M. P. Villar, F. Lloret, et al., "Laser Engineering Nanocarbon Phases Within Diamond for Science and Electronics," *ACS Nano* 18, no. 4 (2024): 2861–2871.

17. P. Németh, K. McColl, L. A. Garvie, et al., "Diaphite-Structured Nanodiamonds With Six- and Twelve-Fold Symmetries," *Diamond and Related Materials* 119 (2021): 108573.

18. A. A. Tsaturyan, E. Kachan, R. Stoian, and J. P. Colombier, "Excited-State Dynamics and Optical Properties of Silica Under Ultrafast Laser Irradiation," *Advanced Physics Research* 4, no. 2 (2025): 2400106.

19. A. Melkonyan, E. Kachan, and J. Colombier, "Thermodynamic Pathways of Silica Glass Densification by Molecular Dynamics Simulations," *Applied Physics A* 131 (2025): 615.

20. B. C. Stuart, M. D. Feit, S. Herman, A. M. Rubenchik, B. W. Shore, and M. D. Perry, "Nanosecond-to-Femtosecond Laser-Induced Breakdown in Dielectrics," *Physical Review B* 53 (1996): 1749–1761, https://link.aps.org/doi/10.1103/PhysRevB.53.1749.

21. M. Rybachuk, B. Ali, and I. V. Litvinyuk, "Ultrashort 30 fs Laser Photoablation for High-Precision and Damage-Free Diamond Machining," *ACS Photonics* 12, no. 9 (2025): 4907–4915.

22. S. Bashir, M. S. Rafique, C. S. Nathala, A. A. Ajami, W. Husinsky, and K. Whitmore, "Pulse Duration and Environmental Effects on the Surface Nanostructuring and Mechanical Properties of Zinc During Femtosecond Laser Irradiation," *Journal of the Optical Society of America B* 37, no. 10 (2020): 2878, https://opg.optica.org/abstract.cfm?URI=josab-37-10-2878.

23. E. Gribaudo, M. Deckart, P. Vlugter, and Y. Bellouard, "Sub-wavelength Femtosecond Laser Based Nanostructuring of Complex Patterns in the Bulk of Fused Silica," *Optics Express* 33, no. 5 (2025): 11529, https://opg.optica.org/abstract.cfm?URI=oe-33-5-11529.

24. A. C. Tam, "Applications of Photoacoustic Sensing Techniques," *Reviews of Modern Physics* 58, no. 2 (1986): 381.

25. S. Manohar and D. Razansky, "Photoacoustics: A Historical Review," *Advances in Optics and Photonics* 8, no. 4 (2016): 586–617, https://opg.optica.org/aop/abstract.cfm?URI=aop-8-4-586.

26. M. A. Lediju Bell, "Photoacoustic Imaging for Surgical Guidance: Principles, Applications, and Outlook," *Journal of Applied Physics* 128, no. 6 (2020): 060904.

27. B. Chu, Z. Chen, H. Shi, et al., "Fluorescence, Ultrasonic and Photoacoustic Imaging for Analysis and Diagnosis of Diseases," *Chemical Communications* 59, no. 17 (2023): 2399–2412.

28. H. H. Huang, S. Juodkazis, and K. Hatanaka, "Correlated Emission of X-Ray and Sound From Water Film Irradiated by Femtosecond Laser Pulses," *Applied Surface Science* 480 (2019): 665–670, https://www.sciencedirect.com/science/article/pii/S0169433219304568.

29. Y. Hayasaki, M. Isaka, A. Takita, S. Hasegawa, and S. Juodkazis, "Photo-Acoustic Sub-Micrometer Modifications of Glass by Pair of Femtosecond Laser Pulses," *Optical Materials Express* 2, no. 5 (2012): 691–699.

30. F. C. P. Masim, W. H. Hsu, H. L. Liu, et al., "Photoacoustic Signal Enhancements From Gold Nano-Colloidal Suspensions Excited by a Pair of Time-Delayed Femtosecond Pulses," *Optical Express* 25, no. 16 (2017): 19497–19507.

31. Y. Hayasaki and T. Miura, "Femtosecond Laser Drilling Controlled With Laser-Generated Ultrasound Pressure," *Applied Physics B* 130 (2024): 220.

32. H. Daido, R. Tateyama, K. Ogura, K. Mima, S. Nakai, and C. Yamanaka, "Measurements of Ablation Pressure and Mass Ablation Rate Using a Target Pendulum and a Thin Foil Target at 10 μm Laser Wavelength," *Japanese Journal of Applied Physics* 22, no. 4A (1983): L248, https://dx.doi.org/10.1143/JJAP.22.L248.

33. H. Daido, R. Tateyama, K. Ogura, et al., "Measurements of Intensity Scaling of Ablation Pressure at 10.6 μm and 1.05 μm Laser Wavelengths," *Japanese Journal of Applied Physics* 23, no. 10R (1984): 1353.

34. K. Terai, H. Daido, M. Fujita, et al., "Hot Electron Energy Distribution in One-Dimensional Cannonball Target at 10.6 μm Laser Wavelength," *Japanese Journal of Applied Physics* 23, no. 7A (1984): L445.

35. C. R. Phipps Jr, T. P. Turner, R. F. Harrison, et al., "Impulse Coupling to Targets in Vacuum by KrF, HF, and CO_2 Single-Pulse Lasers," *Journal of Applied Physics* 64, no. 3 (1988): 1083–1096.

36. K. Gupta, N. K. Jain, and R. Laubscher, "Chapter 6 - Surface Property Enhancement of Gears," in *Advanced Gear Manufacturing and Finishing*, Ed. K. Gupta, N. K. Jain, and R. Laubscher (Academic Press, 2017), 167–196, https://www.sciencedirect.com/science/article/pii/B9780128044605000067.

37. E. G. Gamaly, A. V. Rode, and B. Luther-Davies, "Ablation of solids by Femtosecond Lasers: Ablation Mechanism and Ablation Thresholds for Metals and Dielectrics," *Physics of Plasmas* 18, no. 9 (2002): 949–957.

38. E. G. Gamaly and S. Juodkazis, "Laser–Metal Interaction With a Pulse Shorter Than the Ion Period: Ablation Threshold, Electron Emission and Ion Explosion," *Nanomaterials* 13, no. 11 (2023): 1796, https://www.mdpi.com/2079-4991/13/11/1796.

39. O. Utéza, N. Sanner, B. Chimier, et al., "Surface Ablation of Dielectrics With sub-10 fs to 300 fs Laser Pulses: Crater Depth and Diameter, and Efficiency as a Function of Laser Intensity," *Journal of Laser Micro/Nanoengineering* 5, no. 3 (2010): 238–241.

40. M. Garcia-Lechuga, O. Utéza, N. Sanner, and D. Grojo, "Wavelength-Independent Performance of Femtosecond Laser Dielectric Ablation Spanning Over Three Octaves," *Physical Review Applied* 19 (2023): 044047, https://link.aps.org/doi/10.1103/PhysRevApplied.19.044047.

41. T. A. Labutin, V. N. Lednev, A. A. Ilyin, and A. M. Popov, "Femtosecond laser-Induced Breakdown Spectroscopy," *Journal of Analytical Atomic Spectrometry* 31 (2016): 90–118, https://doi.org/10.1039/C5JA00301F.

42. W. Wu, S. Chai, and Y. Zhou, "Acoustic Characteristics of Laser-Induced Plasmas From the Forming Dynamics Perspective," *Applied Optics* 62, no. 35 (2023): 9375–9382, https://opg.optica.org/ao/abstract.cfm?URI=ao-62-35-9375.

43. C. Alvarez-Llamas, P. Purohit, J. Moros, and J. Laserna, "LIBS-Acoustic Mid-Level Fusion Scheme for Mineral Differentiation Under Terrestrial and Martian Atmospheric Conditions," *Analytical Chemistry* 94, no. 3 (2022): 045009.

44. S. Manohar and D. Razansky, "Photoacoustics: A Historical Review," *Advances in Optics and Photonics* 8, no. 4 (2016): 586–617, https://opg.optica.org/aop/abstract.cfm?URI=aop-8-4-586.

45. S. I. Kudryashov, V. D. Zvorykin, A. A. Ionin, V. Mizeikis, S. Juodkazis, and H. Misawa, "Acoustic Monitoring of Microplasma Formation and Filamentation of Tightly Focused Femtosecond Laser Pulses in Silica Glass," *Applied Physics Letters* 92, no. 10 (2008): 101916, https://pubs.aip.org/apl/article/92/10/101916/145675/Acoustic-monitoring-of-microplasma-formation-and.

46. H. H. Huang, T. Nagashima, K. Kumagai, et al., "THz Radiation From Subwavelength Volumes on Water Surfaces and in Air: Effects of Mass Density Gradients and External Magnetic Fields," *Journal of Physical Chemistry C* 128, no. 35 (2024): 14776–14783.

47. B. Shang, Z. Zhang, N. Zhang, et al., "Acoustic Diagnostics of Femtosecond Laser Filamentation," *IEEE Photonics Technology Letters* 36, no. 7 (2024): 512–515.

48. B. Campanella, S. Legnaioli, S. Pagnotta, F. Poggialini, and V. Palleschi, "Shock Waves in Laser-Induced Plasmas," *Atoms* 7, no. 2 (2019): 57, https://www.mdpi.com/2218-2004/7/2/57.

49. Z. U. Rehman, A. Raza, H. Qayyum, S. Ullah, S. Mahmood, and A. Qayyum, "Characterization of Laser-Induced Shock Waves Generated During Infrared Laser Ablation of Copper by the Optical Beam Deflection Method," *Applied Optics* 61, no. 29 (2022): 8606–8612, https://opg.optica.org/ao/abstract.cfm?URI=ao-61-29-8606.

50. E. Manikanta, L. V. Kumar, P. Venkateshwarlu, C. Leela, and P. P. Kiran, "Effect of Pulse Duration on the Acoustic Frequency Emissions During the Laser-Induced Breakdown of Atmospheric Air," *Applied Optics* 55, no. 3 (2016): 548–555, https://opg.optica.org/ao/abstract.cfm?URI=ao-55-3-548.

51. V. Jukna, S. Albert, C. Millon, et al., "Control of the Acoustic Waves Generated by Intense Laser Filamentation in Water," *Optics Express* 30, no. 6 (2022): 9103–9111, https://opg.optica.org/oe/abstract.cfm?URI=oe-30-6-9103.

52. K. Kumagai, K. Numazawa, and Y. Hayasaki, "Volumetric Cloud Display," *Optica* 12, no. 7 (2025): 1139–1143, https://opg.optica.org/optica/abstract.cfm?URI=optica-12-7-1139.

53. C. Wei and L. Li, "Ultrasonic/Acoustic Methods for Process Monitoring," in *Handbook of Laser Micro- and Nano-Engineering* (Springer, 2020), 1979–2002.

54. S. Staacks, S. Hütz, H. Heinke, and C. Stampfer, "Advanced Tools for Smartphone-Based Experiments: Phyphox," *Physics Education* 53, no. 4 (2018): 045009.

55. S. Staacks and J. Noritzsch, "Akustische phänomene mit der app phyphox untersuchen," in *Schwingungen und Wellen in Alltagskontexten: Impulse für die Unterrichtspraxis und Hochschullehre* (Springer, 2025), 113–122.

56. S. Staacks, S. Hütz, H. Heinke, and C. Stampfer, "Advanced Tools for Smartphone-Based Experiments: Phyphox," *Physics Education* 53, no. 4 (2018): 045009, https://doi.org/10.1088/1361-6552/aac05e.

57. K. Kaleris, Y. Orphanos, S. Petrakis, et al., "Laser-Plasma Sound Sources in Atmospheric Air: A Systematic Experimental Study," *Journal of Sound and Vibration* 570 (2024): 118000, https://linkinghub.elsevier.com/retrieve/pii/S0022460X23004492.

58. H. H. Huang, S. Juodkazis, E. G. Gamaly, V. T. Tikhonchuk, and K. Hatanaka, "Mechanism of Single-Cycle THz Pulse Generation and X-ray Emission: Water-Flow Irradiated by Two Ultra-Short Laser Pulses," *Nanomaterials* 13, no. 18 (2023): 2505, https://www.mdpi.com/2079-4991/13/18/2505.

59. V. Mizeikis, S. Juodkazis, T. Balčiū, et al., "Optical and Ultrasonic Signatures of Femtosecond Pulse Filamentation in Fused Silica," *Journal of Applied Physics* 105, no. 12 (2009): 123106.

60. K. Kaleris, Y. Orfanos, M. Bakarezos, N. Papadogiannis, and J. Mourjopoulos, "Experimental and Analytical Evaluation of the Acoustic Radiation of Femtosecond Laser Plasma Filament Sound Sources in Air," *Journal of the Acoustical Society of America* 146, no. 3 (2019): EL212–EL218.

61. E. G. Gamaly, S. Juodkazis, K. Nishimura, et al., "Laser-Matter Interaction in the Bulk of a Transparent Solid: Confined Microexplosion and Void Formation," *Physical Review B* 73 (2006): 214101.

62. T. Wei and M. Hargather, "A New Blast Wave Scaling," *Shock Waves* 31 (2021): 231–238.

63. R. Goldston and P. Rutherford, *Introduction to Plasma Physics* (Institute of Physics Publishing, 1997).

64. X. L. Liu, X. Lu, X. Liu, et al., "Tightly Focused Femtosecond Laser Pulse in Air: From Filamentation to Breakdown," *Optics Express* 18, no. 25 (2010): 26007–26017, https://opg.optica.org/oe/abstract.cfm?URI=oe-18-25-26007.

65. W. H. Hsu, F. C. P. Masim, A. Balčytis, S. Juodkazis, and K. Hatanaka, "Dynamic Position Shifts of X-Ray Emission From a Water Film Induced by a Pair of Time-Delayed Femtosecond Laser Pulses," *Optics Express* 25, no. 20 (2017): 24109–24118, https://opg.optica.org/oe/abstract.cfm?URI=oe-25-20-24109.

66. K. Hatanaka, T. Ida, H. Ono, et al., "Chirp Effect in Hard X-Ray Generation From Liquid Target When Irradiated by Femtosecond Pulses," *Optics Express* 16, no. 17 (2008): 12650–12657, https://opg.optica.org/oe/abstract.cfm?URI=oe-16-17-12650.

67. J. C. Diels and W. Rudolph, "9 - Diagnostic Techniques," in *Ultrashort Laser Pulse Phenomena (Second Edition)*, second edition, Ed. J. C. Diels and W. Rudolph, (Academic Press, 2006), 457–489, https://www.sciencedirect.com/science/article/pii/B9780122154935500100.

68. P. Gibbon, "Introduction to Plasma Physics," in *CERN-2016-001; the Proceedings of the CAS-CERN Accelerator School: Plasma Wake Acceleration, 23–29 Nov. 2014, Geneva, Switzerland* CERN, Geneva, (CERN 2016), 51–65.

69. P. Gibbon and E. Förster, "Short-Pulse Laser–Plasma Interactions," *Plasma Physics and Controlled Fusion* 38, no. 6 (1996): 769–793.

70. P. Gibbon, *Short Pulse Laser Interactions With Matter: An Introduction* (World Scientific, 2005).

71. N. Zheng, R. Buividas, H. H. Huang, et al., "Laser Machining at High ~ PW/cm^2 Intensity and High Throughput," *Photonics* 11, no. 7 (2024): 598, https://www.mdpi.com/2304-6732/11/7/598.

72. T. Auguste, P. Monot, L. Lompre, G. Mainfray, and C. Manus, "Multiply Charged Ions Produced in Noble Gases by a 1 ps Laser Pulse at $\lambda = 1053$ nm," *Journal of Physics B: Atomic, Molecular and Optical Physics* 25 (1992): 4181–4194.

73. P. Gibbon, "Physics of High-Intensity Laser-Plasma Interactions," in *Proceedings of the International School of Physics "E. Fermi"* 179, no. Laser-Plasma Acceleration (2012): 1–40.

74. O. Koritsoglou, D. Loison, O. Uteza, and A. Mouskeftaras, "Characteristics of Femtosecond Laser-Induced Shockwaves in Air," *Optics Express* 30, no. 21 (2022): 37407–37415, https://opg.optica.org/oe/abstract.cfm?URI=oe-30-21-37407.

Appendix A1: Appendixes

A1.1 | Photons-Per-Atoms in the Interaction Volume

The pulse duration of $t_p = 50$ fs defines the axial extension of the laser pulse $l_l = ct_p = 15$ μm, which is smaller than the axial extent of the focal volume. For the used maximum pulse energy $E_p = 50$ μJ, the photon number is $N_{ph} = \frac{E_p}{hc/\lambda} = 2.01 \times 10^{14}$, here h is the Plank constant. The cylindrical volume they occupy is $V_{ph} = l_l \times \pi r^2$ and is defined by the focusing conditions, where $r = 2.1$ μm is the waist of the beam. The photon volumetric density $\rho_{ph} = \frac{N_{ph}}{V_{ph}} = 9.67 \times 10^{23}$ cm^{-3}. The molecular density of air $\rho_{air}^{(at)} = \rho_{air}\frac{N_a}{M} = 2.64 \times 10^{19}$ cm^{-3}, where N_a is the Avogadro number, $M = 28.84$ g is the molar mass of air, and $\rho_{air} = 1.29$ kg/m^3 (at 20°C). The ratio of photons to molecules in the focal volume occupied by the laser pulse is $\rho_{ph}/\rho_{air}^{(at)} = 3.66 \times 10^4$. A larger density of air can be created using a shock-compressed front using two or more fs-laser pulses [46].

A1.2 | Conditions at Focus in Numbers

The laser intensity $I_p = \frac{1}{2}\varepsilon_0 c E_l^2$ defines the laser electrical field strength E_l (V/m), where c is the speed of light and ε_0 is the permittivity of vacuum. The field strength $E_H = 5.1 \times 10^9$ (V/m) in the hydrogen atom defines the electron–proton interaction force $F = eE_H = k_C\frac{e^2}{r_H^2}$, where e is the electron charge, $r_H = 0.53$ Å is the atomic radius of Hydrogen, k_C is the Coulomb constant [68–70]. The atomic intensity 34.6 PW/cm^2 corresponds to the E_H field strength and this is the peak intensity (twice the average, which is used throughout the text). However, the ionization of Hydrogen occurs at much lower laser fields, at the appearance intensity $I_{ap} = 1.4 \times 10^{14}$ W/cm^2, which is only 0.4% of the atomic intensity [71]. This is derived by a simple physics model [68–70]. When the external electrical field of strength E_{ex} is applied to an atom, the potential is given by $V(x) = -\frac{Ze^2}{x} - eE_{ex}x$ along the x direction. By using the condition $\frac{dV(x)}{dx} = 0$, the position of the potential barrier maximum is $x_{max} = Ze/E_{ex}$; here Z is the atomic number (nuclear charge number). If $V(x_{max}) = E_{ion}$, the critical field strength for barrier suppression ionization (tunneling) is obtained $E_c = \frac{E_{ion}^2}{4Ze^3}$. The corresponding laser intensity defines the *appearance intensity* of the ion, $I_{app} = cE_c^2/(8\pi) = \frac{cE_{ion}^4}{128\pi Z^2 e^6} = 4 \times 10^9 \left[\frac{E_{ion}}{[\text{eV}]}\right]^4 Z^{-2}$ W/cm^2 discussed above for H$^+$ (13.61 eV and $Z = 1$) [72, 73]. For Oxygen O$^+$ $E_{ion} = 13.618$ eV and for N$^+$ 14.53 eV. The tunneling ionization dominates when the Keldysh parameter $\gamma_K \equiv \omega_L\sqrt{2E_{ion}/I_L} < 1$, where ω_L is the cyclic frequency of laser and E_{ion} is the ionization potential.

An air breakdown by 0.5 PW/cm^2 intensity (average) pulses (1030 nm/360 fs) focused by a $NA = 0.4$ objective lens showed shock formation at 100 ps after energy deposition [74]. The threshold intensity of the air breakdown was 80 TW/cm^2. Experimental results showed that shock wave propagation followed the Equation-of-State (EOS) of air $P = (\gamma - 1)[\rho/\rho_0]E_{in}$, where E_{in} is the internal energy per unit volume, which is driving explosion, ρ is air density ($\rho_0 = 1.2 \times 10^{-3}$ g/cm^3 is the unperturbed density), $\gamma = C_p/C_v = 1.4$ is the adiabatic index (or the specific capacity ratio at constant pressure to that at constant volume). The initial pressures reaching kbar-level dropped to tens-of-bar after propagation of a few micrometers with shock velocity ~ 1 km/s after few-ns; the starting conditions were at Mach number ~ 30.

A1.3 | Calibration: Sound to Pressure

Figure A1a shows the specification of the used buzzer for the produced sound pressure at 4 kHz at different voltages. The 10 V bias was used. The sound pressure in dB was recalculated to p (Pa) according to $l_p = 20\log_{10}(p/p_0)$, where the audible limit $p_0 = 20$ μPa. For example, when the buzzer sounded at 10 V and 10 cm from the microphone, the pressure was 80 dB, which corresponded to a 0.1 amplitude (counts) measured by the microphone (Figure A1c).

In a separate experiment, the acoustic signal (pressure) was measured with the microphone being moved from 10 to 100 cm from the buzzer. The dependence of pressure $p \sim 1/x$ was observed, where x is the distance between the buzzer and the microphone. The same acoustic signal amplitude was produced from the buzzer at ~ 1 m and laser-induced spark from 1 cm when only the 4 kHz component was filtered

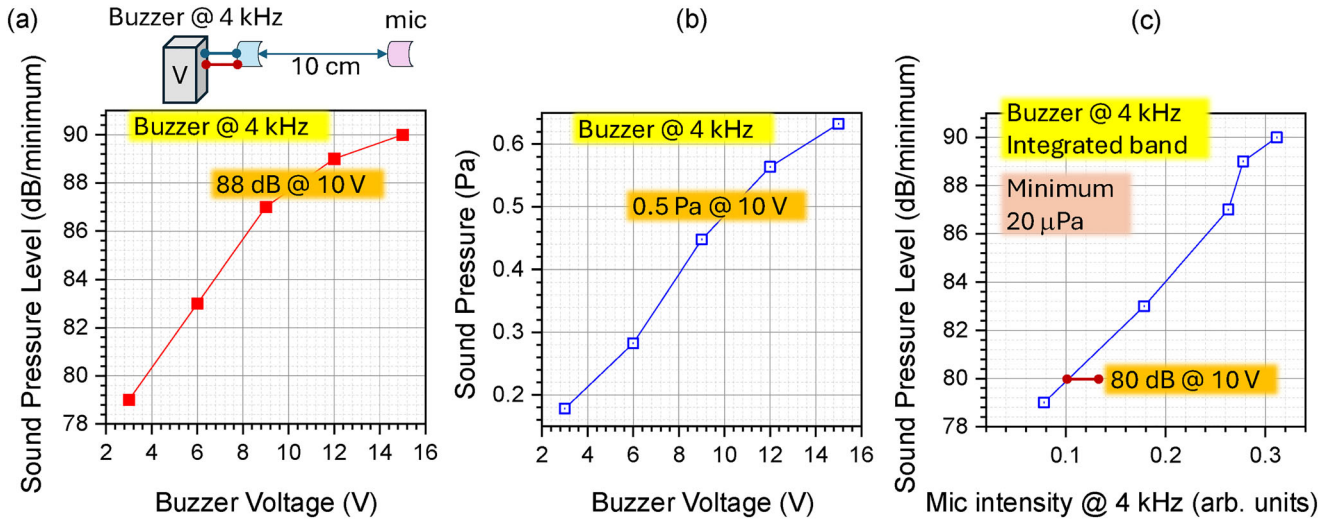

FIGURE A1 | Calibration of the microphone. (a) The sound pressure in dB (referenced to the audible limit of 20 μPa) at different driving voltages of transducer/buzzer (PK-12N40PE-TQ) at 4 kHz; at 10 V and 4.5 mA it produces 88 dB at 4 kHz; top-inset shows schematics of measurements. (b) Sound pressure in Pa at the different buzzer voltages 10 cm from the buzzer. (c) Sound pressure (dB) normalized to the audible limit at 10 cm to the microphone.

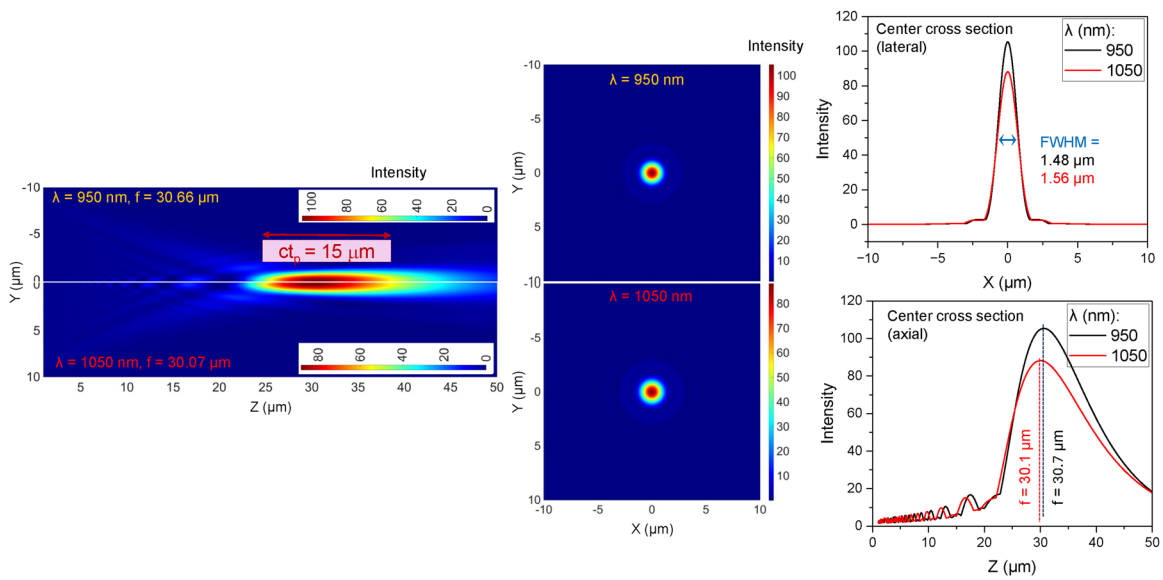

FIGURE A2 | The Rayleigh–Sommerfeld integral calculation (Matlab) for $NA = 0.3$ focusing of 1050 nm and 950 nm wavelength light (those wavelengths are at the spectral edges of 50 fs pulse at FWHM; see Figure 3a). The focal length $f \approx 30$ μm; pulse extent $ct_p = 15$ μm. Calculations are for ideal aberration-free focusing by a lens $NA = 0.3$. Center lateral and axial cross sections are shown on the right-side plots.

from the microphone-detected signal. The described procedure can be used for quantitative calibration of the acoustic signal when required. Noteworthy, the microphone could be more sensitive than the audible limit of 20 μPa (when sound pressure is measured). The sound pressure in dB was used here since it is widely accepted across different fields; however, it is normalized for the audible level (it is a relative measure).

At the employed focusing ($NA = 0.3$), the entire pulse along the propagation direction traversed the focal region with almost the same cross-sectional diameter due to its short 15 μm length, as shown in Figure A2. The sound source originated from the cylindrical volume defined by r and l_l, where ionized air plasma was created and energy was deposited (plasma was sub-critical and transparent rather than reflective).